

Production of gamma rays and neutrinos in the dark jets of the microquasar SS433

M. M. Reynoso^{1*} †, G. E. Romero^{2‡}, and H. R. Christiansen³

¹*Departamento de Física, Facultad de Ciencias Exactas y Naturales, Universidad Nacional de Mar del Plata, Funes 3350, Mar del Plata, 7600, Argentina*

²*Instituto Argentino de Radioastronomía, CONICET, C.C.5, Villa Elisa, 1894, Argentina and Facultad de Ciencias Astronómicas y Geofísicas, Universidad Nacional de La Plata, Paseo del Bosque, La Plata, 1900, Argentina*

³*State University of Ceará, Physics Dept., Av. Paranjana 1700, 60740-000 Fortaleza - CE, Brazil*

Accepted 2008 April 20. Received 2008 April 02; in original form 2008 January 18

ABSTRACT

We study the spectral energy distribution of gamma rays and neutrinos in the precessing microquasar SS433 as a result of pp interactions within its dark jets. Gamma-ray absorption due to interactions with matter of the extended disk and of the star is found to be important, as well as absorption caused by the UV and mid-IR radiation from the equatorial envelopment. We analyze the range of precessional phases for which this attenuation is at a minimum and the chances for detection of a gamma-ray signal are enhanced. The power of relativistic protons in the jets, a free parameter of the model, is constrained by HEGRA data. This imposes limits on the gamma-ray fluxes to be detected with instruments such as GLAST, VERITAS and MAGIC II. A future detection of high energy neutrinos with cubic kilometer telescopes such as IceCube would also yield important information about acceleration mechanisms that may take place in the dark jets. Overall, the determination of the ratio of gamma-ray to neutrino flux will result in a key observational tool to clarify the physics of heavy jets.

Key words: stars: binaries: individual: SS433 – gamma-rays: theory – neutrinos.

1 INTRODUCTION

The famous and enigmatic microquasar SS433 has been matter of investigation for more than two decades. Consisting of a donor star feeding mass to a black hole, it presents two oppositely directed, precessing jets with hadronic content¹. We refer to the relativistic collimated outflows as ‘dark’ jets (Gallo et al. 2005) since the very high kinetic luminosity $L_k \sim 10^{39}$ erg s^{−1} (Dubner et al. 1998) appears as the dominant power output of the ejected material, having imprinted a deformation on the supernova remnant W50.

Most of the radiative output of the system is observed in the UV and optical bands, whereas the X-ray emission detected is ~ 1000 lower than the kinetic energy of the jets, probably due to a screening effect with an equatorial outflow (Revnivtsev et al. 2006; Marshall et al. 2006). The gamma-ray emission above 0.8 TeV has been constrained by HEGRA to be $\Phi_\gamma < 8.93 \times 10^{-13}$ cm^{−2}s^{−1} (Aharonian et al.

2005) whereas the neutrino flux upper limit according to AMANDA-II data is $\Phi_\nu < 0.21 \times 10^{-8}$ cm^{−2}s^{−1} (Halzen 2006).

In previous hadronic models for high energy emission from microquasars, relativistic protons in the jets interact with target protons from the stellar wind of the companion star (Romero et al. 2003; Christiansen et al. 2006; Orellana et al. 2007). Since in the case of SS433 there is no evidence of such a strong stellar wind, in this work we investigate the possible production of gamma rays and neutrinos resulting from pp interactions between relativistic and cold protons within the jets themselves.

2 PRELIMINARIES

The binary SS433, distant 5.5 kpc from the Earth, displays two mildly relativistic jets ($v_b \approx 0.26c$) that are oppositely directed and precess in cones of half opening angles of $\theta \approx 21^\circ$. The line of sight makes an angle $i = 78^\circ$ with the normal to the orbital plane and a time-dependent angle $i_j(t)$ with the approaching jet (see Fig. 1). Assuming that $\psi(t)$ is the precessional phase of the approaching jet, we shall follow the convention that when $\psi = 0$

* E-mail: mreynoso@mdp.edu.ar (MMR)

† Fellow of CONICET

‡ Member of CONICET

¹ Iron lines with a shift corresponding to a velocity of $v \sim 0.26c$ have been detected, for instance, by Migliari et al. (2002).

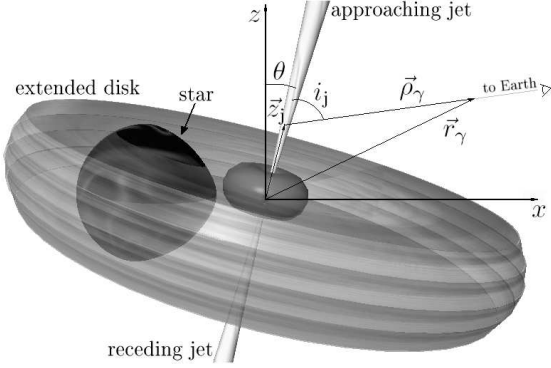


Figure 1. Schematic view of the SS433. The *approaching* jet is most of the time closest to our line of sight and the *receding* one is oppositely directed.

the mentioned jet points closer to the Earth. Then, when $\psi = 0.5$, it has performed half of the precession cycle and it makes its largest angle with the line of sight. The mass loss rate in the jets is $\dot{m}_j = 5 \times 10^{-7} M_\odot \text{yr}^{-1}$, the period of precession is 162 d and the orbital period is 13.1 d (Fabrika 2004). The donor star and the compact object are thought to be embedded in a thick expanding disk which is fed by a wind from the supercritical accretion disk around the black hole (Zwitter et al. 1991). This equatorial envelope is perpendicular to the jets and according to Fabrika (2004) we assume that it has a half opening angle $\alpha_w \approx 30^\circ$, a mass loss rate $\dot{M}_w \approx 10^{-4} M_\odot \text{yr}^{-1}$ and a terminal velocity $v_w \sim 1500 \text{ km s}^{-1}$. Also, this extended disk has been recognized as the origin of both the UV and mid-IR emission (Gies et al. 2002a; Fuchs et al. 2005) which can cause significant absorption of gamma-rays as discussed in Reynoso et al. (2008).

The spectral identification of the companion star has been difficult due to the presence of the extended disk, since the star is often partially or totally obscured by it. After convenient observations at specific configurations of precession and orbital phases it has become quite clear that the star is an A-supergiant (Hillwig et al. 2004; Barnes et al. 2006; Cherepashchuk et al. 2005). We assume the masses of the components as derived from INTEGRAL observations (Cherepashchuk et al. 2005), $M_{\text{bh}} = 9 M_\odot$ and $M_\star = 30 M_\odot$ for the black hole and star respectively. This corresponds to an orbital separation $a \simeq 79 R_\odot$ for a zero-eccentricity orbit as it is the case for SS433. Since the star is believed to fill its Roche lobe, the implied radius according to Eggleton (1983) is $R_L \simeq 38 R_\odot$.

2.1 Outline of the jet model

We assume that a magneto-hydrodynamic mechanism for jet ejection operates in SS433, that is, ejection is realized through the conversion of magnetic energy into matter kinetic energy. The magnetic energy density is supposed to be in equipartition with the kinetic energy density of the ejected particles, so that the corresponding magnetic field along the jet is given by

$$B(z_j) = \sqrt{8\pi e_j}, \quad (1)$$

where the kinetic energy density is

$$e_j = \frac{\dot{m}_j E_k}{m_p v_b \pi R_j^2(z_j)}. \quad (2)$$

Here E_k is the classical kinetic energy of a jet proton with velocity v_b and $R_j(z)$ is the jet radius at the height z_j along the jet axis.

The jets are modeled as cones with a half opening angle $\xi_j \approx 0.6^\circ$ (Marshall et al. 2006). Assuming an initial jet radius $R_0 = R_j(z_0) \approx 5 R_{\text{Sch}}$, where $R_{\text{Sch}} = 2GM_{\text{bh}}/c^2$, we find the injection point as $z_0 = R_0 / \tan \xi_j \simeq 1.3 \times 10^9 \text{ cm}$. Since the jets are heavy as compared to other similar objects, it is reasonable to admit that they are cold matter dominated. In this case, we assume that a small fraction of relativistic or hot particles are confined by the cold plasma. According to Bosch-Ramon et al. (2006) the pressure of cold particles is greater than that of the relativistic ones if the ratio of cold to hot particles is less than 1/1000, and this condition will be greatly satisfied provided that the luminosity carried by relativistic particles is required to be smaller than the total kinetic luminosity of the jet.

Particle acceleration is supposed to take place via diffusive acceleration by internal shocks converting bulk kinetic energy into random kinetic energy. According to the standard model for non-relativistic shock acceleration (e.g. Blandford & Eichler 1987 and references therein) we expect that the relativistic proton spectrum is given by a power-law, $N'_p(E'_p) = K_0 E'^{-\alpha}_p$ at $z_j = z_0$, where the spectral index is the standard value for first order diffusive shock acceleration, $\alpha = 2$. The flux of these protons hence evolves with z_j as

$$J'_p(E'_p) = \frac{cK_0}{4\pi} (z_0/z_j)^2 E'^{-\alpha}_p$$

in the jet frame, which transformed to the observer frame (Purmohammad & Samimi 2001) reads

$$J_p(t, E_p, z_j) = \frac{cK_0}{4\pi} \left(\frac{z_0}{z_j} \right)^2 \times \frac{\Gamma^{-\alpha+1} (E_p - \beta_b \sqrt{E_p^2 - m_p^2 c^4} \cos i_j)^{-\alpha}}{\sqrt{\sin^2 i_j + \Gamma^2 \left(\cos i_j(t) - \frac{\beta_b E_p}{\sqrt{E_p^2 - m_p^2 c^4}} \right)^2}} \equiv \left(\frac{z_0}{z_j} \right)^2 \tilde{J}_p(E_p, t), \quad (3)$$

where $i_j(t)$ is the angle between the jet axis and the line of sight, $\beta_b = 0.26$, and $\Gamma = [1 - \beta_b^2]^{-1/2}$ is the jet Lorentz factor. The normalization constant K_0 is obtained by specifying the fraction of power carried by the relativistic protons, q_{rel} ,

$$\pi R_0^2 \int_{E'_p(\text{min})}^{E'_p(\text{max})} J'_p(E'_p) E'_p dE'_p = q_{\text{rel}} L_k, \quad (4)$$

so that

$$K_0 = \frac{4q_{\text{rel}} L_k}{c R_0^2 \ln \left(\frac{E'_p(\text{max})}{E'_p(\text{min})} \right)}, \quad (5)$$

where we take $E'_p(\text{min}) \approx 1 \text{ GeV}$ and the maximum proton energy $E'_p(\text{max})$ will be determined in the next section. We

shall adopt, for the illustrative predictions of neutrino and gamma-ray fluxes, a tentative value $q_{\text{rel}} = 10^{-4}$, but a full discussion of the possible range for this parameter will be presented in Sect. 5.

3 HADRONIC PROCESSES IN THE JETS

Relativistic protons in the jets are subject to different mechanisms that can make them lose energy. In this section we analyze the energy range where pp collisions are the dominant cooling process that will produce the corresponding gamma rays and neutrinos in SS433.

3.1 Acceleration

The acceleration rate of protons up to an energy E_p can be estimated as (Begelman et al. 1990):

$$t_{\text{accel}}^{-1} \approx \eta \frac{ceB}{E_p}, \quad (6)$$

where $\eta \sim \beta_b^2$ is the acceleration efficiency. Clearly, as long as the latter rate is greater than the total loss rate for a given energy, protons will be effectively accelerated up to that energy.

As mentioned in Sect. 2.1, we assume that the protons are accelerated at shocks produced by collisions of plasma outflows with different bulk velocities. In the frame of the shock, the conservation equations imply that the upstream velocity is significantly higher than the downstream velocity, i.e., $v_u/v_d = (\gamma_{\text{heat}} + 1)/(\gamma_{\text{heat}} - 1) = \xi$, with γ_{heat} the ratio of specific heats and ξ the compression factor. In this way, the two regions may be regarded as two converging flows. The Fermi first order acceleration mechanism then operates to produce a power law particle spectrum, which is essentially independent of the microphysics involved. Strong shocks ($\xi \sim 4$) can be non-relativistic as it is the case, for instance, in supernova remnants and colliding wind massive binaries. In the case of sub-relativistic jets, strong shocks are expected as suggested by the non-thermal synchrotron radio spectra observed from the jets of microquasars (Fender 2004). Non-linear effects like shock modification by the pressure of the relativistic particles or magnetic field effects can result in a variety of spectral indexes. The reader is referred to the recent paper by Rieger et al. (2006) on Fermi acceleration in astrophysical jets, which includes a section on mildly relativistic microquasar outflows.

The acceleration of protons proceeds only for protons with a threshold energy that allows the diffusive acceleration process to take place (Rieger et al. 2006). Then, only the supra-thermal tail of the Maxwellian distribution of cold protons will be affected by the process (Bosch-Ramon et al. 2006). This has the result that just a small fraction of the total power carried by the jet is converted to relativistic particles.

3.2 Cooling rates and maximum particle energy

The density of cold protons at a distance z_j from the black hole in each jet is

$$n_p(z_j) \simeq \frac{\dot{m}_j}{\pi [R_j(z_j)]^2 m_p v_b}. \quad (7)$$

These cold protons serve as targets for the relativistic ones, so that the rate of pp collisions in the jet is given by

$$t_{pp}^{-1} = n_p(z_j) c \sigma_{pp}^{(\text{inel})}(E_p) K_{pp}, \quad (8)$$

where the inelasticity coefficient is taken to be $K_{pp} \approx 1/2$ since on average, the leading proton loses half of its total energy per collision.

The cross section for inelastic pp interactions can be approximated by (Kelner et al. 2006)

$$\sigma_{pp}^{(\text{inel})}(E_p) = (34.3 + 1.88L + 0.25L^2) \times \quad (9)$$

$$\left[1 - \left(\frac{E_{\text{th}}}{E_p} \right)^4 \right]^2 \times 10^{-27} \text{ cm}^2, \quad (10)$$

where $L = \ln(E_p/1000 \text{ GeV})$ and $E_{\text{th}} = 1.22 \text{ GeV}$.

Cooling by $p\gamma$ interactions can take place mainly via photopion production ($\gamma p \rightarrow p\pi^i$) and pair production ($\gamma p \rightarrow p e e^+$) (Begelman et al. 1990). The corresponding cooling rate can be obtained from (Atoyan & Dermer 2003)

$$t_{p\gamma}^{-1} = \int_{\frac{E'_{\text{th}}}{2\gamma_p}}^{\infty} dE \frac{cn_{\text{ph}}(E)}{2\gamma_p^2 E^2} \int_{E_{\text{th}}}^{2\gamma_p E} dE_r \sigma_{p\gamma} K_{p\gamma} E_r dE_r, \quad (11)$$

where $E'_{\text{th}} \approx 150 \text{ MeV}$, γ_p is the Lorentz factor of the proton, $n_{\text{ph}}(E)$ represents the density of target photons, $\sigma_{p\gamma}$ will be the inelastic cross section appropriate for photopion and photopair creation, and $K_{p\gamma}$ is the corresponding inelasticity coefficient.

Photopion production will occur when protons collide with X-ray photons, for which, based on Cherepashchuk et al. (2005), we adopt a Bremsstrahlung X-ray distribution for $2 \text{ keV} < E < 100 \text{ keV}$,

$$n_X(E) = L_X \frac{e^{-E/(kT_e)}}{4\pi z_j^2 E^2} \text{ (erg}^{-1} \text{ cm}^{-3} \text{)}, \quad (12)$$

where $kT_e \approx 30 \text{ keV}$ and $L_X = 10^{36} \text{ erg s}^{-1}$. These X-ray photons are considered to be originated in a corona surrounding the inner accretion disk, as suggested in Cherepashchuk et al. (2005).

The cross section for photopion production is approximated by (Atoyan & Dermer 2003)

$$\sigma_{p\gamma}^{(\pi)} = \Theta(E_r - 200 \text{ MeV}) \Theta(500 \text{ MeV} - E_r) 3.4 \times 10^{-28} \text{ cm}^2 \\ + \Theta(E_r - 500 \text{ MeV}) 1.2 \times 10^{-28} \text{ cm}^2, \quad (13)$$

and the inelasticity coefficient for photopion production is

$$K_{p\gamma}^{(\pi)} = \Theta(E_r - 200 \text{ MeV}) \Theta(500 \text{ MeV} - E_r) 0.2 \\ + \Theta(E_r - 500 \text{ MeV}) 0.6. \quad (14)$$

The contribution of the $e^- e^+$ pair creation process to the total $p\gamma$ cooling rate is calculated also using Eq. (11), but the soft photon density in this case includes also the contribution associated with the UV emission from the extended disk,

$$n_{\text{ph}}(E) = n_{\text{UV}}(E, \Omega) \frac{\pi R_{\text{out}}^2}{z_j^2} + n_X(E).$$

Based on the discussion in Gies et al. (2002a), the UV photons with wavelengths in the range (1000 Å, 10000 Å)

correspond to a blackbody distribution with $T_{UV} = 21000$ K. Hence, we take the corresponding radiation density as

$$n_{UV}(E, \Omega) = 2E^2(hc)^{-3}(e^{E/kT_{UV}} - 1)^{-1}. \quad (15)$$

For this process we consider the expressions for cross section and inelasticity given in Begelman et al. (1990):

$$\sigma_{p\gamma}^{(e)} = 5.8 \times 10^{-28} \text{ cm}^2 \left[3.11L' - 8.07 + \frac{(2m_e c^2/E)^2 (2.7L' - L'^2 + 0.67L'^3 + 0.55) - (2m_e c^2/E)^4 (0.19L' + 0.13) - (2m_e c^2/E)^6 (0.01L')}{3.11L' - 8.07} \right] \quad (16)$$

and

$$K_{p\gamma}^{(e)} = 4 \frac{m_e^2 c^2}{m_p E_r} \left[\frac{-8.78 + 5.51 L' - 1.61 L'^2 + 0.69 L'^3}{3.11 L' - 8.07} \right] \quad (17)$$

with $L' = \ln\left(\frac{2E}{m_e c^2}\right)$.

The accelerated protons can also lose energy in the form of synchrotron radiation at a rate

$$t_{\text{sync}}^{-1} = \frac{4}{3} \left(\frac{m_e}{m_p} \right)^3 \frac{\sigma_T B^2}{m_e c 8\pi} \gamma_p, \quad (18)$$

and via Inverse Compton scatterings with X-ray and UV photons at a rate

$$t_{\text{IC}}^{-1} = \frac{4}{3} \left(\frac{m_e}{m_p} \right)^3 \frac{\sigma_T e_{\text{ph}}}{m_e c} \gamma_p, \quad (19)$$

where

$$e_{\text{ph}} = \int_{E_{\text{min}}}^{m_p^2 c^4 / E_p} n_{\text{ph}}(E) E dE$$

is the corresponding density of energy in target soft photons (Begelman et al. 1990).

It is also expected that the accelerated protons will suffer adiabatic losses because of the expansion undergone by the jets. The corresponding adiabatic cooling rate can be written as (see e.g. Bosch Ramon et al. 2006)

$$t_{\text{adiab}}^{-1} = \frac{2}{3} \frac{v_b}{z_j} \quad (20)$$

We show the obtained results for the acceleration and cooling rates at the base of each jet ($z_j = z_0$) in Fig. 2.

As it can be seen from this plot, the expected cooling rates for $p\gamma$ and Inverse Compton interactions are found to be negligible. We infer that the protons which can be effectively accelerated up to energies below

$$E_p^{(\text{max})} \approx 3.4 \times 10^6 \text{ GeV}, \quad (21)$$

will cool efficiently mainly via pp collisions at z_0 . For higher energies, synchrotron losses become dominant. On the other hand, as z_j increases, adiabatic losses also grow and the maximum proton energy at which pp collisions dominate can change along the jets.

The absolute maximal energy for protons at a given z_j , $E_p^{(\text{abs})}$ (see Fig. 3) is obtained from $t_{\text{accel}}^{-1} = t_{pp}^{-1} + t_{\text{adiab}}^{-1} + t_{\text{sync}}^{-1} + t_{\text{IC}}^{-1} + t_{p\gamma}^{-1}$.

The size constraint, implying that the proton gyro-radius has to be smaller than the radius of the jet, i.e. $E_p < E_p^{(\text{size})} = eR_j B \approx 3 \times 10^8 \text{ GeV}$, does not happen to limit the energy of the protons at the bases of the jets. Note

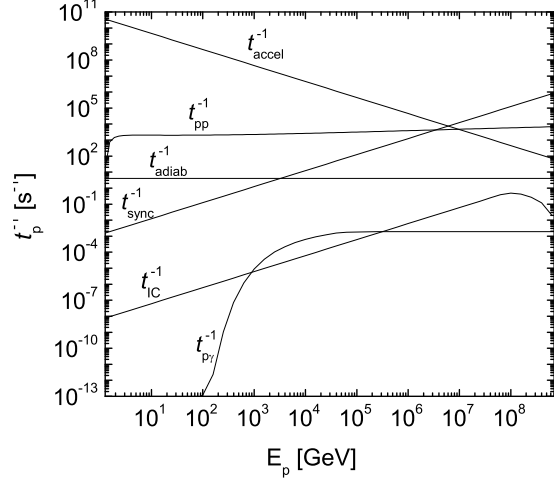


Figure 2. Proton accelerating and cooling rates at the base of the jets.

also that we have the same value of $E_p^{(\text{size})}$ for larger values of z_j along the jets because $B \propto R_j^{-1}$. Nevertheless, the size constraint will limit the energy of the accelerated protons at distances $z_j \gtrsim 3 \times 10^{12} \text{ cm}$ from the black hole (see Fig. 3).

In the (z_j, E_p) region where pp collisions dominate the cooling mechanism, the condition $t_{pp}^{-1} > t_{\text{sync}}^{-1} + t_{\text{adiab}}^{-1} + t_{\text{IC}}^{-1} + t_{p\gamma}^{-1}$ must hold. This region is indicated in the shaded zone of Fig. 3. It can be seen that the maximum energies for efficient cooling through pp interactions are $E_p^{(\text{max})} \sim 3 \times 10^6 \text{ GeV}$ for $z_j < z_1$, where $z_1 \approx 10^{12} \text{ cm}$.² Therefore, the jet will become essentially cold and observationally dark, unless some re-acceleration mechanism could operate (e.g. mediated by re-collimation shocks or terminal shocks).

It is also worth noting that decreasing the parameter q_{rel} does not change the maximum proton energy given by (21) since in that case the target proton density is essentially unchanged and so is the pp cooling rate. This allows us to take q_{rel} as a free parameter that can be easily factored out in all of our predictions for gamma-ray and neutrino signals.

3.3 High-energy gamma rays from pp interactions

The collision of a certain number of high-energy protons with cold protons in the jets will cause the production of secondary gamma rays and neutrinos. Following the treatment of Kelner et al. (2006), which is based on SIBYLL simulations of pp interactions including perturbative QCD effects, the spectrum of produced gamma-rays with energy

² Since the necessary maximal energy in equation (5) has to be expressed in the frame comoving with the jet, we take $E_p'^{(\text{max})} \simeq \Gamma(E_p^{(\text{max})} - \beta_j \sqrt{E_p^{(\text{max})^2 - m_p^2 c^4})$, where $E_p^{(\text{max})} \approx 3.4 \times 10^6 \text{ GeV}$ at the base of the jet.

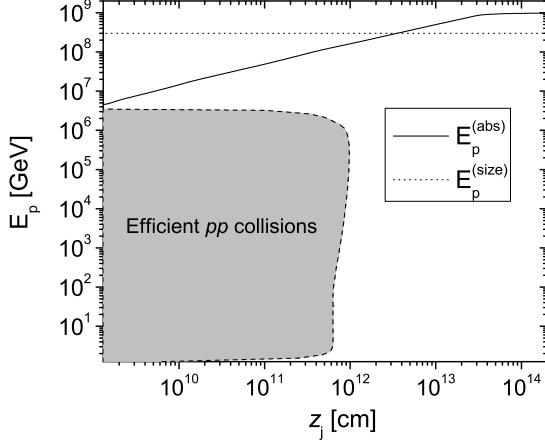


Figure 3. The region in the (z_j, E_p) plane where pp interactions are the dominant cooling mechanism is indicated in gray. The absolute maximum proton energy (solid line) and the maximum proton energy from the size constraint (dotted line) are also shown.

$E_\gamma = xE_p$ for a primary proton with energy E_p reads

$$F_\gamma(x, E_p) = B_\gamma \frac{\ln x}{x} \left(\frac{1 - x^{\beta_\gamma}}{1 + k_\gamma x^{\beta_\gamma} (1 - x^{\beta_\gamma})} \right)^4 \times \left[\frac{1}{\ln x} - \frac{4\beta_\gamma x^{\beta_\gamma}}{1 - x^{\beta_\gamma}} - \frac{4k_\gamma \beta_\gamma x^{\beta_\gamma} (1 - 2x^{\beta_\gamma})}{1 + k_\gamma x^{\beta_\gamma} (1 - x^{\beta_\gamma})} \right], \quad (22)$$

where

$$B_\gamma = 1.3 + 0.14 L + 0.011 L^2 \quad (23)$$

$$\beta_\gamma = \frac{1}{1.79 + 0.11 L + 0.008 L^2} \quad (24)$$

$$k_\gamma = \frac{1}{0.801 + 0.049 L + 0.014 L^2}, \quad (25)$$

with $L = \ln(E_p/1 \text{ TeV})$.

For $E_\gamma > 100 \text{ GeV}$, we shall consider the gamma-ray emissivity at a height z_j along the jets as

$$\frac{dN_\gamma(t, E_\gamma, z_j)}{dE_\gamma} = \int_{x_{\min}}^{x_{\max}} \sigma_{pp}^{\text{inel}} \left(\frac{E_\gamma}{x} \right) J_p \left(t, \frac{E_\gamma}{x}, z_j \right) \times F_\gamma \left(x, \frac{E_\gamma}{x} \right) dx \quad (26)$$

$$\equiv \left(\frac{z_0}{z_j} \right)^2 \frac{d\tilde{N}_\gamma(t, E_\gamma)}{dE_\gamma} \quad (27)$$

in units $\text{GeV}^{-1} \text{s}^{-1}$. The integration limits x_{\min} and x_{\max} are chosen in order to cover the proton energy range where pp collisions dominate at each z_j , as shown in Fig. 3. On the other hand, for $E_\gamma < 100 \text{ GeV}$, we shall consider, as suggested in Kelner et al. (2006), the emissivity obtained using the δ -functional approximation

$$\frac{dN_\gamma(t, E_\gamma, z_j)}{dE_\gamma} = 2 \int_{E_{\min}}^{E_{\max}} \frac{q_\pi(t, E_\pi, z_j)}{\sqrt{E_\pi^2 - m_\pi^2 c^4}} dE_\pi, \quad (28)$$

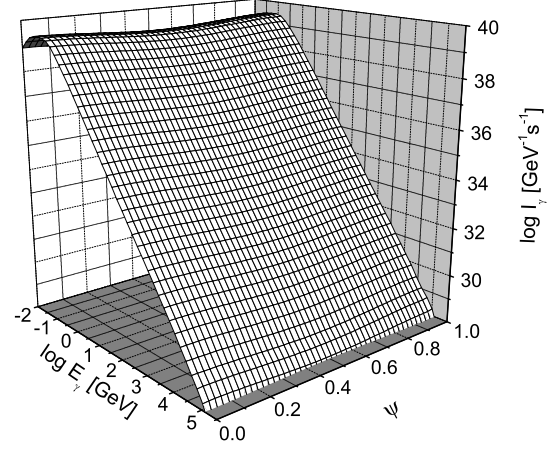


Figure 4. Spectral intensity of gamma-rays produced in the approaching jet as a function of the precessional phase and the gamma-ray energy.

where $E_{\min} = E_\gamma + \frac{m_\pi^2 c^4}{4E_\gamma}$, $E_{\max} = K_\pi(E_p^{(\max)} - m_p c^2)$, and

$$q_\pi(t, E_\pi, z_j) = \frac{\bar{n}}{K_\pi} \sigma_{pp}^{\text{inel}} (m_p c^2 + \frac{E_\pi}{K_\pi}) \times J_p(t, m_p c^2 + \frac{E_\pi}{K_\pi}, z_j). \quad (29)$$

Here, $K_\pi \approx 0.17$ is the fraction of the proton kinetic energy that is transferred to the gamma rays or leptons. The number of produced pions, \bar{n} , is a free parameter of the model that is fixed by requiring continuity of the gamma-ray emissivity at $E_\gamma = 100 \text{ GeV}$.

The spectral intensity of gamma rays emitted from the jet can be obtained from

$$I_\gamma(t, E_\gamma) = \int_{z_0}^{z_1} \pi(z_j \tan \xi)^2 n_p \frac{dN_\gamma(t, E_\gamma, z_j)}{dE_\gamma} dz_j \quad (30)$$

$$\simeq \frac{\dot{m}_j z_0}{m_p v_b} \frac{d\tilde{N}_\gamma(t, E_\gamma)}{dE_\gamma}. \quad (31)$$

We show the obtained result for gamma rays produced in the approaching jet in Fig. 4.

3.4 High-energy neutrino emission from pp interactions

Neutrinos are produced by the decay of the charged pions resulting from pp interactions,

$$\pi^- \rightarrow \mu^- \bar{\nu}_\mu \rightarrow e^- \nu_\mu \bar{\nu}_e \bar{\nu}_\mu \quad (32)$$

$$\pi^+ \rightarrow \mu^+ \nu_\mu \rightarrow e^+ \bar{\nu}_\mu \nu_e \nu_\mu \quad (33)$$

In the present context, the equipartition condition implies a strong magnetic field at the base of the jet. Hence, the charged mesons will undergo important losses due to synchrotron radiation. In order to find the local steady distribution of the parent charged pions at fixed E_p , we have considered the following transport equation

$$\frac{db_\pi(E_\pi) F_\pi(E_\pi)}{dE_\pi} + \frac{F_\pi(E_\pi)}{\tau_\pi(E_\pi)} = F_\pi^{\text{(inj)}}(E_\pi) t_{pp}^{-1}. \quad (34)$$

Here, $\tau_\pi = \tau_\pi^{(0)} \gamma_\pi$, with $\tau_\pi^{(0)} = 2.6 \times 10^{-8}$ s, is the pion mean lifetime, $b_\pi(E_\pi) = E_\pi(t_{\text{sync}}^{-1}(E_\pi, z_j) + t_{\text{adiab}}^{-1}(z_j))$, and

$$F_\pi^{(\text{inj})}(E_\pi) = 4\alpha B_\pi x_\pi^{\alpha-1} \left(\frac{1 - x_\pi^\alpha}{1 - r x_\pi^\alpha (1 - x_\pi^\alpha)} \right)^4 \times \left(\frac{1}{1 - x_\pi^\alpha} + \frac{r(1 - 2x_\pi^\alpha)}{1 + r x_\pi^\alpha (1 - x_\pi^\alpha)} \right) \left(1 - \frac{m_\pi c^2}{x_\pi E_p} \right)^{1/2} \quad (35)$$

is the distribution of injected pions per pp collision (Kelner et al. 2006), where $x_\pi = E_\pi/E_p$, $B_\pi = a + 0.25$, $a = 3.67 + 0.83L + 0.075L^2$, $r = 2.6/\sqrt{a}$, and $\alpha = 0.98/\sqrt{a}$. The transport equation (34) includes the effects of decays and energy loss of pions in the left member and the injection of pions in the right side.

The corresponding solution can be written as

$$F_\pi(E_\pi) = \int_{E_\pi}^{E_p} \frac{F_\pi^{(\text{inj})}(E') t_{pp}^{-1}}{|b_\pi(E_\pi)|} \times \exp \left\{ \frac{1}{b_z E_\pi} - \frac{1}{b_z E'} + \frac{a_z}{b_z^2} \log \left(\frac{E_\pi}{E'} \right) + \frac{a_z}{b_z^2} \log \left(\frac{b_z + a_z E'}{b_z + a_z E_\pi} \right) \right\} dE', \quad (36)$$

where

$$a_z = \frac{4}{3} \left(\frac{m_e}{m_\pi} \right)^3 \frac{\sigma_T B^2(z_j) \tau_\pi^{(0)}}{8\pi m_e c (m_\pi c^2)^2},$$

$$b_z = \frac{2 v_b}{3 z_j} \frac{\tau_\pi^{(0)}}{m_\pi c^2}.$$

The spectrum of high energy neutrinos from the direct decay of the steady distribution of pions is then

$$F_\nu(x, E_p) = \frac{2}{\lambda} \int_0^\lambda F_\pi \left(\frac{E_\nu}{x}, E_p \right) \frac{dx}{x}, \quad (37)$$

where $x = E_\nu/E_p$ and $\lambda = 0.427$.

As it is the case for the pions, the muons also undergo synchrotron and adiabatic losses. In this case, their mean lifetime is much longer ($\tau_\mu = \tau_\mu^{(0)} \gamma_\mu$ with $\tau_\mu^{(0)} = 2.2 \times 10^{-6}$ s). This implies that these leptons will lose most of their energy before decaying, especially at the inner parts of the jets, where most of the emission is originated. This can be seen in Fig. 5, where we show the decay rate τ_μ^{-1} and the loss rate $t_{\mu, \text{loss}}^{-1} = t_{\mu, \text{sync}}^{-1} + t_{\mu, \text{adiab}}^{-1}$ as a function of the muon energy, for different values of z_j . According to this figure, muons with energies beyond 1 TeV will be present in the jets only at $z_j > 10z_0$. Hence, since we are interested in neutrinos with energies $E_\nu > 1$ TeV, the neutrino emission is attenuated due to the synchrotron losses in our model. The above equations show that to a good approximation we can safely neglect the contribution from muon decays at high energies.

The neutrino emissivity can then be expressed as

$$\frac{dN_\nu(t, E_\nu, z_j)}{dE_\nu} = \int_{x_{\min}}^{x_{\max}} \sigma_{pp}^{\text{inel}} \left(\frac{E_\nu}{x} \right) J_p \left(t, \frac{E_\nu}{x}, z_j \right) \times F_\nu \left(x, \frac{E_\nu}{x} \right) dx \quad (38)$$

$$\equiv \left(\frac{z_0}{z_j} \right)^2 \frac{d\tilde{N}_\nu(t, E_\nu)}{dE_\nu}. \quad (39)$$

The total neutrino spectral intensity emitted in the jet thus

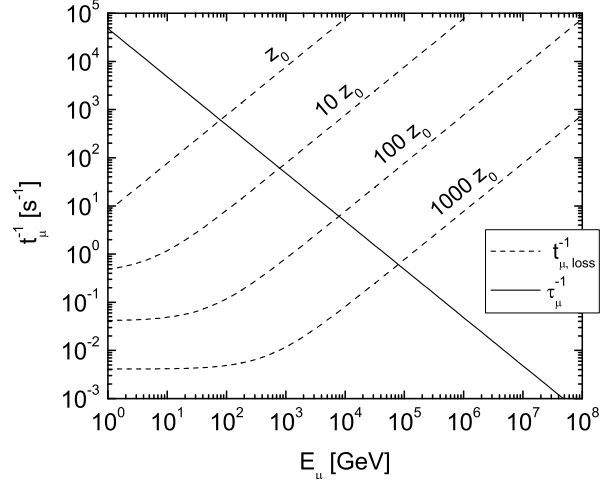


Figure 5. Decay and loss rates for muons at different values of z_j .

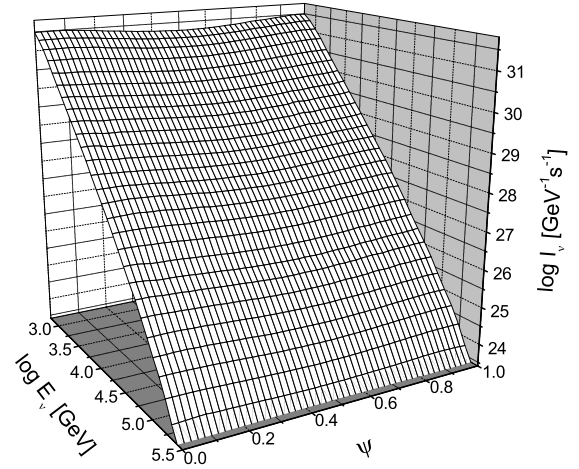


Figure 6. Spectral intensity of neutrinos produced in the approaching jet as a function of the precessional phase and the neutrino energy.

reads

$$I_\nu(t, E_\nu) \simeq \frac{\dot{m}_j z_0}{m_p v_b} \frac{d\tilde{N}_\nu(t, E_\nu)}{dE_\nu}. \quad (40)$$

We show the result obtained for neutrinos produced in the approaching jet in Fig. 6.

4 OPACITY TO GAMMA-RAY PROPAGATION

The various mechanisms at work for gamma-ray absorption in the microquasar SS433 have recently been studied in Reynoso et al. (2008). Absorption can occur via $\gamma\gamma$ interactions with ambient soft photons and by γN interactions with disk and star matter.

In the first case, absorption occurs through interactions with low energy photons originated in the star and in the extended disk. These take place in the pair creation channel,

and the corresponding optical depth results from integration of

$$d\tau_{\gamma\gamma} = (1 - \hat{e}_\gamma \cdot \hat{e}_{\text{ph}}) n_{\text{ph}}(E, \Omega') \sigma_{\gamma\gamma} d\rho_\gamma dE d\cos\theta' d\phi' \quad (41)$$

as described in Reynoso et al. (2008). Here, $d\rho_\gamma$ is the differential path followed by the gamma ray, E is the soft photon energy, \hat{e}_γ is the unit vector in the direction of the gamma ray, and $\hat{e}_{\text{ph}} = (\sin\theta' \cos\phi', \sin\theta' \sin\phi', \cos\theta')$ is the vector directed along the direction of the soft photons. The cross section for the process $\gamma\gamma \rightarrow e^+e^-$ is

$$\sigma_{\gamma\gamma}(E_\gamma, E) = \frac{\pi r_0^2}{2} (1 - \xi^2) \times \left[2\xi(\xi^2 - 2) + (3 - \xi^4) \ln \left(\frac{1 + \xi}{1 - \xi} \right) \right],$$

where r_0 is the classical electron radius and

$$\xi = \left[1 - \frac{2(m_e c^2)^2}{E_\gamma E (1 - \hat{e}_\gamma \cdot \hat{e}_{\text{ph}})} \right]^{1/2}. \quad (42)$$

The radiation density of soft photons, in units $\text{cm}^{-3} \text{erg}^{-1} \text{sr}^{-1}$, is $n_{\text{ph}}(E, \Omega') = 2E^2 (hc)^{-3} (e^{E/kT} - 1)^{-1}$ with $T = 8500$ K for the starlight photons and with $T = 21000$ K for the UV photons from the extended disk. The mid-IR emission is characterized by a radiation density $n_{\text{ph}}(E, \Omega') \approx F_{\text{IR}} d^2 / (hc E \pi r_\gamma^2 \cos(0.62\pi))$, with $F_{\text{IR}} = 2.3 \times 10^{-23} (\lambda/\mu\text{m})^{-0.6}$ for $2 \mu\text{m} < \lambda < 12 \mu\text{m}$ (Fuchs et al. 2005).

As for the absorption due to interactions with matter, the important effects are photopion production $\gamma N \rightarrow \pi^i \gamma$ and photopair production $\gamma N \rightarrow Ne^+e^-$, where N represents a nucleon. This last effect has not been previously considered, so it will be taken into account in the present work. We assume that the star has a matter density

$$\rho_\star(r) = \frac{M_\star}{4\pi R_\star r^2} \Theta(r - R_\star),$$

where r is the distance from the gamma-ray position to the center of the star. For the extended disk, we consider that matter density is given by

$$\rho_w(r_\gamma) = \frac{\dot{M}_w}{v_w \Delta \Omega r_\gamma^2},$$

for $60^\circ < \theta_Z < 120^\circ$, where θ_Z is the polar angle in a coordinate system with its Z -axis directed along the approaching jet axis (for details, see Reynoso et al. 2008). The γN contribution to the optical depth is

$$\tau_{\gamma N}(z_j) = \int_0^\infty \sigma_{\gamma N} \frac{(\rho_\star + \rho_w)}{m_p} d\rho_\gamma, \quad (43)$$

where $\sigma_{\gamma N} = \sigma_{p\gamma}^{(\pi)} + \sigma_{p\gamma}^{(e)}$ can be obtained from equations (13) and (16).

In Fig. 7 we show the total optical depth as a function of the precessional phase for different energies of gamma rays originated at the injection point z_0 of the approaching jet. A very similar result is obtained the base of the receding jet, since z_0 is much smaller than any other size scale of the system. We clearly see the peaks of extreme absorption produced every time the star eclipses the emission region. The dependance of the total optical depth on the distance to the black hole z_j is also shown in Fig. 8 for gamma rays of energy $E_\gamma = 1$ TeV coming from the approaching jet.

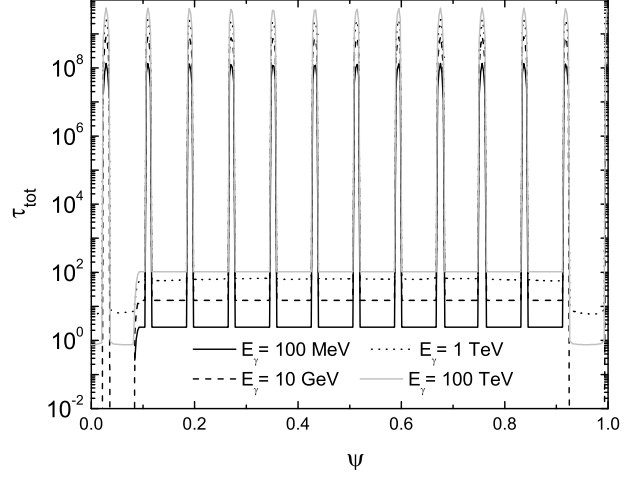


Figure 7. Total optical depth as a function of the precessional phase for gamma rays of different energies originated at the injection point z_0 of the approaching jet.

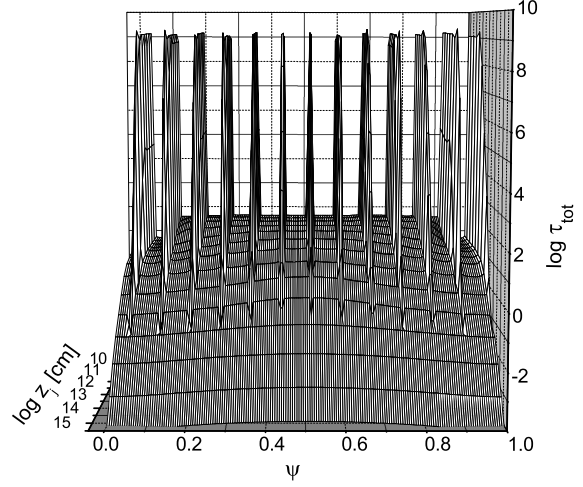


Figure 8. Total optical depth as a function of the precessional phase and z_j for gamma-rays with $E_\gamma = 1$ TeV originated in the approaching jet.

5 NEUTRINO AND GAMMA-RAY DETECTABILITY

The spectral intensities shown in Figs. 4 and 6 were obtained for $q_{\text{rel}} = 10^{-4}$ without considering absorption. However, it is of course necessary to include the absorption effects to see how they affect the produced fluxes that may arrive to the Earth.

The differential gamma-ray flux to be observed from each jet can be obtained as

$$\frac{d\Phi_\gamma(t, E_\gamma)}{dE_\gamma} = \frac{1}{4\pi d^2} \int_{z_0}^{z_1} \pi(z_j \tan \xi)^2 n_p \times \quad (44)$$

$$\frac{dN_\gamma(t, E_\gamma, z_j)}{dE_\gamma} e^{-\tau_{\text{tot}}(t, E_\gamma, z_j)} dz_j. \quad (45)$$

We show in Fig. 9 the joint contribution of both jets

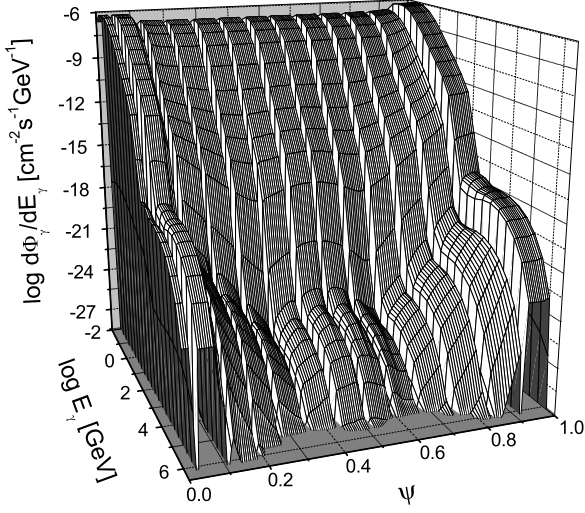


Figure 9. Differential gamma-ray flux arriving at Earth as a function of precessional phase and energy.

to the differential gamma-ray flux considering $q_{\text{rel}} = 10^{-4}$. Here, the absorption effects and the precessional phase behavior have become manifest in the spectrum (c.f. Fig. 4).

As for neutrinos, although they undergo only weak interactions, we can estimate the corresponding neutrino optical depth using an expression analogous to (43),

$$\tau_{\nu N}(\vec{z}_j) = \int_0^\infty \sigma_{\nu N} \frac{(\rho_\star + \rho_w)}{m_p} d\rho_\gamma. \quad (46)$$

Here the total $\nu_\mu N$ cross section can be approximated for $E_\nu > 1$ TeV as $\sigma_{\nu N}(E_\nu) \approx 10^{\alpha_\nu(E_\nu)} \text{cm}^2$, with

$$\alpha_\nu(E_\nu) = -38.42 + 1.46 \log\left(\frac{E_\nu}{\text{GeV}}\right) - 0.116 \log^2\left(\frac{E_\nu}{\text{GeV}}\right) + 0.0041 \log^3\left(\frac{E_\nu}{\text{GeV}}\right).$$

The differential neutrino flux arriving to Earth can therefore be estimated as

$$\frac{d\Phi_\nu(t, E_\nu)}{dE_\nu} = \frac{1}{8\pi d^2} \int_{z_0}^{z_1} \pi(z_j \tan \xi)^2 n_p \times \frac{dN_\nu(t, E_\nu, z_j)}{dE_\nu} e^{-\tau_{\nu N}(t, E_\nu, z_j)} dz_j. \quad (47)$$

Notice that an additional $1/2$ factor has been put in order to take into account the reduction in the muon neutrino flux due to flavor oscillations over astrophysical distances (e.g. Athar et al. 2005). The result for the differential neutrino flux from the two jets with $q_{\text{rel}} = 10^{-4}$ is shown in Fig. 10 as a function of precessional phase and neutrino energy.

We can now integrate the differential fluxes in energy to appreciate the precessional dependance of the signals,

$$\Phi(\psi) = \int_{E^{(\text{min})}}^{E^{(\text{max})}} \frac{d\Phi}{dE} dE.$$

It is interesting to explore the energy ranges that are expected to be covered with different instruments. In the case of neutrinos with $E_\nu > 1$ TeV, in view of possible detection with IceCube, we obtain the flux shown in Fig. 11,

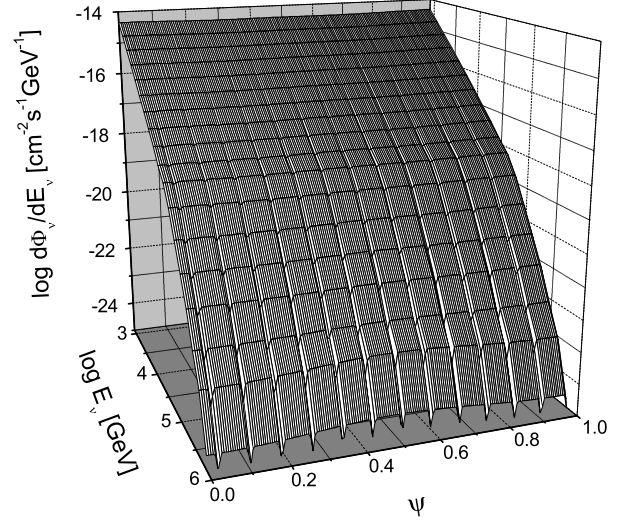


Figure 10. Differential neutrino flux arriving at Earth as a function of precessional phase and energy.

where the contributions from the two jets appear separately. It is also included in that figure the value of the upper limit that can be extracted from AMANDA-II data, $\Phi_\nu^{(\text{lim})}(E_\nu > 1 \text{ TeV}) = 2.1 \times 10^{-11} \text{cm}^{-2} \text{s}^{-1}$ (Halzen 2006), which agrees with recently published experimental results (Achterberg et al. 2007). The expected sensitivity for a km^3 neutrino telescope such as IceCube, $\Phi_\nu^{(\text{km}^3)}(E_\nu > 1 \text{ TeV}) \approx 2 \times 10^{-12} \text{cm}^{-2} \text{s}^{-1}$ for three years of operation, is also shown in Fig. 11 (Halzen 2006; Distefano et al. 2007; Aiello et al. 2007).

As for gamma rays, the sensitivity expected for GLAST is $\Phi_\gamma^{(\text{GLAST})} \simeq 6 \times 10^{-9} \text{cm}^{-2} \text{s}^{-1}$ at $100 \text{ MeV} < E_\gamma < 300 \text{ GeV}$ ³, while for Cherenkov telescopes such as VERITAS and MAGIC II we consider a sensitivity $\Phi_\gamma^{(\text{Cher})} \simeq 9 \times 10^{-12} \text{cm}^{-2} \text{s}^{-1}$ for energies $E_\gamma > 100 \text{ GeV}$ (Carmona et al. 2007). We show in Fig. 12 the integrated gamma-ray fluxes expected for $q_{\text{rel}} = 10^{-4}$ in the mentioned energy ranges, as compared with the respective sensitivities. There, the contributions from the two jets are plotted separately. We also include in the lower panel the results corresponding to $E_\gamma > 800 \text{ GeV}$, since they allow a comparison with the upper limit given by HEGRA for that energy range (Aharonian et al. 2005), $\Phi_\gamma^{(\text{lim})}(E_\gamma > 0.8 \text{ TeV}) = 8.93 \times 10^{-13} \text{cm}^{-2} \text{s}^{-1}$.

According to our model, the most favorable range of precessional phases for the gamma-ray detection is found to be between $\psi \lesssim 0.09$ and $\psi \gtrsim 0.91$, as it can be seen from Fig. 12. This corresponds to the cases when the extended disk is so much open in our direction that the gamma rays emitted at the innermost regions can escape without having to travel through the thick extended disk, undergoing only $\gamma\gamma$ absorption.

However, since the observations by HEGRA were not performed exclusively at the dates of favorable precessional phases (Aharonian et al. 2005), we compare the value of the HEGRA cut with that of the averaged flux over one pre-

³ See the official NASA GLAST webpage, <http://glast.gsfc.nasa.gov/science/instruments/table1-1.html>

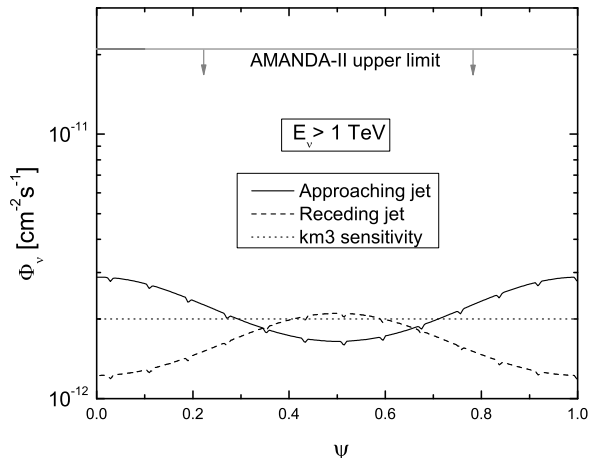


Figure 11. Neutrino fluxes arriving at Earth with $E_\nu > 1$ TeV as a function of the precessional phase. The contributions of the two jets are shown separately, solid line for the approaching jet and dashed line for the receding one. The upper limit from AMANDA-II data and the expected km³ sensitivity are shown in grey solid line and dotted line respectively.

cession cycle, according to our model. Thus, the implied maximum value allowed by the HEGRA limit for the free parameter q_{rel} is

$$q_{\text{rel}}^{(\text{max})} = 10^{-4} \frac{\Phi_\gamma^{(\text{lim})}}{\langle \Phi_\gamma \rangle} \approx 2.9 \times 10^{-4},$$

which is below the maximum value allowed by the AMANDA II limit.

Given that this parameter can be linearly factored out in our equations provided that $q_{\text{rel}} \ll 1$, which is guaranteed for the allowed cases, we can plot the predictions for the different averaged fluxes as a function of this parameter and compare them with the expected sensitivities for the different instruments.

This is done in Fig. 13, where the mean neutrino flux as a function of q_{rel} is shown in the upper panel as compared with the AMANDA-II upper limit and with the expected sensitivity for km³ neutrino telescopes such as IceCube. The gamma-ray fluxes for $100 \text{ MeV} < E_\gamma < 300 \text{ GeV}$ and for $E_\gamma > 100 \text{ GeV}$ averaged in the above mentioned range of favorable precessional phases are shown in the middle and lower panels of the same figure, as a function of q_{rel} . The vertical line indicates the bound $q_{\text{rel}}^{(\text{max})}$ derived from HEGRA observations, which is clearly more restrictive than the one implied by the AMANDA-II upper limit.

6 DISCUSSION AND SUMMARY

We have studied the high-energy emission originated in the dark jets of the microquasar SS433. A small fraction of its particle contents are relativistic protons that collide with the cold ions within the jets, producing gamma rays and neutrinos after pion decay processes. We found that up to distances $\sim 10^{12} \text{ cm}$ from the black hole, protons with energies below $\sim 3 \times 10^6 \text{ GeV}$ will cool dominantly via pp interactions. The ratio of the power carried by relativistic protons to the total kinetic power of the jet, q_{rel} , was kept as a free

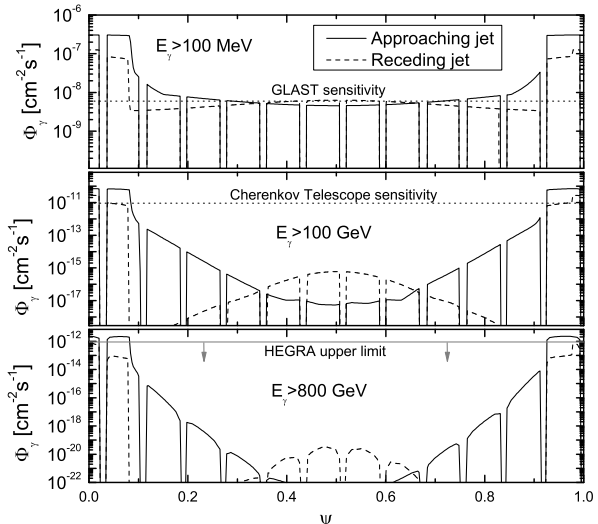


Figure 12. Gamma-ray fluxes arriving at Earth as a function of the precessional phase for $100 \text{ MeV} < E_\gamma < 300 \text{ GeV}$ in the upper panel, for $E_\gamma > 100$ in the middle panel, and for $E_\gamma > 800 \text{ GeV}$ in the lower panel. The contributions of the two jets are shown separately: solid line for the approaching jet and dashed line for the receding one.

parameter of the model (for illustrative purposes we have used $q_{\text{rel}} = 10^{-4}$ in the figures).

We have calculated the spectrum of gamma rays and high-energy neutrinos based on the formulae given by Kelner et al. (2006). We have considered the cooling of the charged pions and muons produced, and we have found that the high-energy neutrino emission is attenuated by synchrotron losses. Adding the contribution from both jets, we have obtained the total gamma-ray spectral intensity of SS433. The gamma radiation will be largely absorbed while leaving the inner regions the system by means of several processes. This will mainly occur through interaction with matter of the star and extended disk, leading to significant photopair production. UV and mid-IR photons originated in the extended disk are also expected to cause important absorption via $\gamma\gamma$ annihilations.

The total optical depth is found to depend on the precessional phase in such a way that when the approaching jet is pointing away from the Earth, at $\psi \sim 0.5$, the extended disk blocks the emitting region and the absorption is strongest. In particular, in the range of precessional phases between $\psi \gtrsim 0.91$ and $\psi \lesssim 0.09$, the gamma rays originated at the base of the jets will travel to the Earth without having to pass through the equatorial disk. With the conservative assumption that this outflowing disk presents a large half opening angle $\alpha_w = 30^\circ$, the mentioned range of favorable precessional phases gives a total of $\sim 29 \text{ d}$ for optimal detectability. Since, according to Gies et al. (2002b), $\psi = 0$ occurred on 2002 June 5, it follows that the next upcoming opportunities to achieve detection will be centered around the following dates every 162 d: 2008 August 20, 2009 January 29, 2009 July 10, etc. As mentioned above, the exact duration along which the favorable conditions may hold, depends on the half opening angle of the extended disk, which might be smaller than what was assumed. In that case, the observational window would be broader

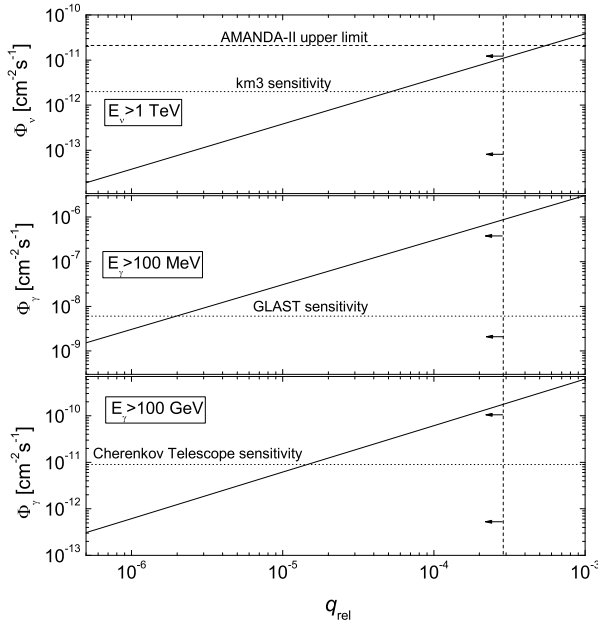


Figure 13. Dependence on q_{rel} of the different flux predictions: average neutrino flux (*upper panel*) and average gamma-ray flux for $100 \text{ MeV} < E_\gamma < 300 \text{ GeV}$ (*middle panel*) and for $E_\gamma > 100 \text{ GeV}$ (*lower panel*). The vertical line indicates the maximum possible value of q_{rel} derived from HEGRA observations. The corresponding sensitivities are also shown (see the text for details).

The observations by HEGRA imply a maximum value for the free parameter q_{rel} in $\sim 3 \times 10^{-4}$. Given the expected sensitivity of the next km^3 neutrino telescopes generation, it will be possible to test our model down to values $\sim 5 \times 10^{-5}$ in three years of operation. An extended range of this parameter will be probed by gamma-ray observations with GLAST and Cherenkov telescopes, especially if performed on the favorable dates.

We conclude that its dark jets can be the possible site for both gamma-ray and neutrino production in SS433. Since most of the high-energy flux is generated in the inner jets, gamma-ray absorption will make detection with Cherenkov telescopes like VERITAS and MAGIC-II difficult but not impossible if attempted at the favorable dates when the approaching jet is closest to the line of sight. Actually, there are much better prospects for gamma-ray observation with GLAST and neutrino detection with IceCube also seems promising. The determination of the gamma-ray to neutrino flux ratio would allow to estimate q_{rel} unambiguously, yielding crucial information about acceleration mechanisms taking place in the jets.

ACKNOWLEDGMENTS

We thank an anonymous referee for his/her constructive comments on this work. G.E.R. is supported by the Argentine agencies CONICET (PIP 452 5375) and ANPCyT (PICT 03-13291 BID 1728/OC-AR). additional support is provided by the Ministerio de Educación y Ciencia (Spain) under grant AYA2007-68034-C03-01, FEDER funds. H.R.C.

is supported by FUNCAP, Brazil, and M.M.R. is supported by CONICET, Argentina. M.M.R. is also thankful to O.A. Sampayo for very useful discussions.

REFERENCES

- Achterberg A. et al., 2007, *Phys. Rev. D* 75, 102001
- Aharonian F. et al., 2005, *A&A*, 439, 635
- Aiello S. et al., 2007 *Astropart. Phys.*, 28, 1
- Athar H., Kim C.S., Lee J., 2007, *Mod. Phys. Lett. A*, 21, 1049
- Atayan A.M., Dermer C.D., 2003, *ApJ* 586, 79
- Barnes A.D. et al., 2006, *A&As*, 365, 296
- Becker P.A., Kafatos M., 1995, *ApJ*, 453, 83
- Begelman M.C., Rudak B., Sikora M., 1990, *ApJ*, 362, 38
- Begelman M.C., King A.R., Pringle J.E., 2006, *MNRAS*, 370, 399
- Blandford R., Eichler D., 1987, *Phys. Rep.*, 154, 1
- Bosch-Ramon V., Romero G.E., Paredes J.M., 2006 *A&A*, 447, 263
- Carmona E. et al, 2007, 30th International Cosmic Ray Conference, arXiv:0709.2959v1
- Cherepashchuk A.M. et al., 2005, *A&A*, 437, 561
- Christiansen H.R., Orellana M., Romero G.E., 2006 *Phys. Rev. D*, 73, 063012
- Distefano C., 2007 *Astrophys. Space Sci.*, 309, 415
- Dubner G.M., Holdaway M., Goss W.M., Mirabel I.F., 1998, *AJ*, 116, 1842
- Eggleton P.P., 1983, *ApJ*, 268, 368
- Fabrika S., 2004, *Astrophys. Space Phys. Rev.*, 12, 1
- Fender R., 2006, in: *Compact stellar X-ray sources*, Walter Lewin & Michiel van der Klis (eds.), Cambridge University Press, Cambridge, p. 381
- Fuchs Y., Miramond L.K., Ábrahám P., 2006, *A&A*, 445, 1041
- Gallo E. et al., 2005, *Nature* 436, 819
- Gies D.R., McSwain M.V., Riddle R.L., Wang Z., Wiita P.J., Wingert D.W., 2002, *ApJ*, 566, 1069
- Gies D.R., Huang W., McSwain M.V., 2002, *ApJ*, 578, L67
- Halzen F., 2006, *Eur. Phys. J.*, C46, 669
- Hillwig T.C. et al., 2004, *ApJ*, 615, 422
- Kelner S.R., Aharonian F.A., Bugayov V.V., 2006, *Phys. Rev. D*, 74, 034018
- Marshall H.L., Canizares C.R., Schulz N.S., 2002, *ApJ*, 564, 941
- Migliari S., Fender R., Méndez M., 2002, *Science*, 297, 1673
- Orellana M., et al., 2007, *A&A*, 476, 9
- Purmohammad D., Samimi J., 2001, *A&A*, 371, 61
- Revnivtsev M. et al., 2006, *A&A*, 447 545
- Reynoso M.M., Christiansen H.R., Romero G.E., 2008, *Astropart. Phys.*, 28, 565
- Rieger F.M., Bosch-Ramon V., Duffy P., 2007, *Ap&SS*, 309, 119
- Romero G.E., Torres D.F., Kaufman-Bernadó M.M., Mirabel I.F., 2003, *A&A*, 410, L1
- Romero G.E., Christiansen H.R., Orellana M., 2005, *ApJ*, 632, 1093
- Zwitter T., Calvani M., D’Odorico S., 1991, *A&A*, 251, 92